Journal of Materials Chemistry A

Some Aspects of the Charge Transfer Dynamics in Nanostructured WO3 Films

Journal:	*Journal of Materials Chemistry A*
Manuscript ID	TA-ART-08-2015-006887.R1
Article Type:	Paper
Date Submitted by the Author:	09-Oct-2015
Complete List of Authors:	Caramori, Stefano; University of Ferrara, Chemistry Bignozzi, C A; University of Ferrara, Chemistry Cristino, Vito; Università di Ferrara, Chemistry Argazzi, Roberto; ISOF-CNR, Carli, Stefano; University of Ferrara, Chemistry Molinari, Alessandra; University of Ferrara, Chemistry Boaretto, Rita; University of Ferrara, Chemistry Marinello, Sabrina; University of Ferrara, Chemistry Meda, Laura; Istituto Donegani, ENI, CHIFIS

Some Aspects of the Charge Transfer Dynamics in Nanostructured WO_3 Films

Vito Cristino,[a] Sabrina Marinello,[a] Alessandra Molinari,[a] Stefano Caramori,[a]* Stefano Carli,[a] Rita Boaretto,[a] Roberto Argazzi,[b] Laura Meda,[c] and Carlo Alberto Bignozzi[a]*

(a) Department of Chemical and Pharmaceutical Sciences, University of Ferrara, Via Fossato di Mortara 17, 44121 Italy.
(b) CNR/ISOF c/o Department of of Chemical and Pharmaceutical Sciences, Via Fossato di Mortara 17, 44121 Italy
(c) Istituto ENI Donegani, Via Fauser 4, 28100, Novara, Italy

(*)Stefano Caramori: cte@unife.it
(*)Carlo Alberto Bignozzi: g4s@unife.it

Abstract

The photoanodic response of two different types of nanocrystalline WO_3 electrodes prepared by following either the sol gel approach or the accelerated anodization route was explored in sulfate containing electrolytes with the aim of exploring the mechanism of charge separation at WO_3/electrolyte interfaces. Combined evidences by Electrochemical Impedance Spectroscopy and Transient Absorption Spectroscopy indicate that the hole transfer occurs through the valence band and that, under applied bias, the voltage drop involves predominantly the space charge layer of the semiconductor, controlling the photocurrent via potential-induced variations of hole density at the surface of WO_3. OH radicals were found among the primary water oxidation intermediates, and are partly responsible for mediated back recombination. The generation of hydroxyl radicals suggests, however, that WO_3 based materials can find promising applications for environmental photoremediation under visible light, promoting ·OH mediated oxidation of impervious contaminants. In principle, the removal of ·OH by organic scavengers will also optimize the photocurrent generation in photoelectrochemical cells where the generation of hydrogen can be coupled to environmental decontamination.

Introduction

The use of semiconductor materials represents one of the most promising way to harvest solar energy resulting in the production, with unitary quantum yield,[1, 2] of charge carriers which can be used to drive redox reactions at the semiconductor interface in contact with either liquid electrolytes, vapor or gas phases, triggering the direct conversion of solar energy into chemical energy. Both the yield of the fuel forming reactions in photoelectrochemical cells, where oxygen and hydrogen ideally result from the splitting of the water molecule, and the efficiency of the photocatalytic pathways, aimed at either the demolition of environmental contaminants or at the production of useful chemical intermediates for synthetic chemistry,[3] are primarily dependent on the competition between interfacial charge transfer and recombination, on charge trapping events, and on the nature of the chemical intermediates which form at the heterogeneous interface under illumination. Metal oxide semiconductors, prominently TiO_2 (anatase and rutile),[4] monoclinic WO_3,[5] and α-hematite (α-Fe_2O_3)[6] have attracted a considerable interest in photocatalysis and in photoelectrochemistry due their chemical and photochemical stability, relative abundance, environmental safety and band gap energetics suitable to the production of charge carriers with sufficient free energy to drive a variety of redox reactions. As such, WO_3 is a promising material for photoelectrochemical and photocatalytic applications, since, unlike TiO_2, harvests a reasonable portion of the visible spectrum and displays charge transfer and conductivity properties superior to α-hematite electrodes, as demonstrated by comparative tandem cell efficiencies with optimized materials.[7]

WO_3 can be prepared by a variety of techniques aimed at the production of nanostructured interfaces, which optimize the interfacial area[8] as well as electrical interconnection among the nanoparticles/nanostructures. These methods include, but are not limited to, sol-gel, hydrothermal and electrophoretic processes,[9-13] electrochemical anodization,[14-17] rf sputtering,[18, 19] pulsed laser deposition[20] and evaporation.[21] It has been recently demonstrated that WO_3 constitutes one of the best platforms for hosting $BiVO_4$ and realizing $WO_3/BiVO_4$ heterojunctions with nearly unitary IPCE[22]. Attempts to further modify its electronic properties by modification/doping with Al^{3+},[23] Gd^{3+},[24] Nb^{3+},[25] HfO_2,[26] Fe^{3+},[27] have been recently reported, demonstrating some success, at least at a comparative level with respect to the unmodified baseline materials realized in the same laboratories. This is attributed to a combination of factors ranging from improved semiconductor conductivity, increased interfacial charge transfer rates and passivation of surface recombination centers, whose specific contribution to the overall improved electrode performance is often difficult to be individually separated and addressed.

In order to further improve the charge transfer properties of WO_3, its coupling to a Fe based molecular catalyst was explored,[28] showing a permanent performance improvement of the WO_3/catalyst assembly over unmodified WO_3, despite the disappearance of the Fe complex from the semiconductor surface, a fact that was attributed to the formation of some other active catalytic species following demolition of the molecular precursor upon prolonged photoelectrolysis.

Although it is often assumed that oxygen evolves at the WO_3 surface following illumination at anodic potentials,[29] Mi et al.,[30] by using a luminescent probe, found nearly no oxygen evolved in sulfate containing electrolytes, pointing out that the oxidation of the anions may be the predominant hole scavenging pathway in acidic conditions. Such finding is in relative disagreement with a report by Hill[31] which found oxygen production yields of the order of 35 and 72 % at pH 1 and 3 respectively in Na_2SO_4 containing electrolytes.

Thus, in view of the current efforts to realize photoresponsive materials, hybrid interfaces, and solar devices with improved efficiency, it is important to address the active mechanisms at the basis of the charge separation processes at the WO_3/electrolyte interface, to individuate the nature and the fate of the main chemical intermediates resulting from hole injection into the electrolyte, to understand the effect of the applied potential bias on the charge separation and charge recombination kinetics with the more general aim of providing diagnostic tools which can be useful for the investigation of new WO_3 based materials.

In this contribution we report on the photoanodic response of two different types of nanocrystalline WO_3 electrodes prepared by following either the sol gel approach (transparent films on FTO ((Fluorine Tin Oxide) glass) or the accelerated anodization route, leading to oxide films grown on tungsten foils (opaque electrodes). Sulfate based electrolytes, where different cations were present, including alkyl-ammonium cations (Tetra-Butyl-Ammonium (TBA^+) and Tetra-Methyl-Ammonium (TMA^+)) in which a significantly increased photoanodic current was observed, were employed. The conventional DC photoelectrochemical investigation was complemented by Electrochemical Impedance Spectroscopy (EIS), while Electronic Paramagnetic Resonance (EPR) with spin traps helped to individuate the radical intermediates produced by WO_3 under visible illumination. Transient Absorption Spectroscopy (TAS) carried out on transparent electrodes under applied potential bias allowed to individuate the spectroscopic signature of the photoholes and to outline the role of the applied bias in influencing the lifetimes and the surface concentration of the photogenerated charge carriers in different electrolytes.

The combined evidences gained by these techniques provide a strong indication that the space charge layer developed within WO_3 plays an active role in driving the charge separation across the semiconductor/electrolyte interface, and that OH radicals are among the primary

oxidation intermediates, constituting, as a matter of fact, also active recombination centers. The evidence gained from this study suggests that WO_3 may find a successful application not only in photoelectrochemical cells for solar fuel production but also as a material for environmental photoremediation under visible light, promoting ·OH mediated oxidation reactions via valence band hole injection.

Experimental

Materials. Unless otherwise stated all materials were used as received. Methanol 99.8%, ethylene and propylene carbonate(98% and 99% respectively), HCl 37%, Hydrogen sulfate salts ($TBAHSO_4$ 97%, $NaHSO_4$ 90%, $KHSO_4$ 97%, $TMAHSO_4$ 98%) were purchased from Aldrich and Alfa Aesar. $LiHSO_4$ was prepared by combining stoichiometric amounts of LiOH 98% (Aldrich) and H_2SO_4 95-97% (Aldrich). Na_2WO_4 99-101%, NH_4F 98%, NMF 99% (N-Methyl-formamide) and tungsten foils 99.95% (0.05 mm) were purchased from Alfa Aesar. Tungsten sheets were ultrasonically cleaned with Alconox (Aldrich) prior to use in the anodization bath. Conductive glass slides (FTO TEC 8) from Pilkington were cleaned by sonication in isopropanol 99.8% and in Alconox solution before their use as conductive substrates for transparent WO_3 films. Spin traps DMPO 97% (5,5' dimethyl-pyrrolin-N-oxide) and pbn 99.5% (n-tert-butyl-α-phenylnitrone)) were from Aldrich. Aqueous electrolytes were prepared with Millipore water.

AFM. Tapping mode AFM imaging was carried out on both colloidal and anodic WO_3 substrates by using a multimode Bruker-Digital Instruments-Veeco Nanoscope III equipped with Bruker RTESP n-silicon tip. Flattened imaged areas (both 3 x 3 micron and 1x1 micron) were treated with Nanoscope Analysis 1.5 software to extract relevant topological and morphological information on the nanocrystalline substrates.

Photoelectrochemical measurements. Different Potentiostats from EcoChemie (PGSTAT 30, 302/N+FRA2 and 101) and Amel were available and were indifferently used for DC measurements. Potentiodynamic JV curves were collected in the dark and under illumination (ABET sun simulator AM1.5G, ca. 0.1 W/cm^2), using a three electrode configuration (WO_3/SCE/Pt wire), by sweeping the voltage in the anodic range, typically from 0 to 1.5-1.7 V vs SCE at a scan rate of 20 mV/s. IPCE[32] was collected under the monochromatic illumination generated by the coupling of a Luxtel 175 W Xe lamp to an Applied Photophysics monochromator, using a spectral bandwidth of 10 nm and a constant potential bias of 1.5 V vs SCE. Photocurrent transients were obtained under potentiostatic control by chopping the excitation light with a Scitec Instrument LTD 320 C chopper at a maximum frequency of 20Hz and a custom built sector disk. Photocurrent peak

FWHM (Full Width at Half Maximum) was used here as a comparative parameter for the estimation of the charge transit time across the film

Impedance data under potentiostatic conditions were collected by using the Nova 1.11 software under sun simulated illumination by using a single sinusoidal perturbation having an amplitude of 20 mV in the frequency range 10^5-10^{-2} Hz, and integrating over three cycles. The potential was sampled at 20 mV intervals in the anodic region where the steepest ascending portion of the JV characteristic was observed, typically 0.2-0.6 V vs SCE. The complete scan of the potential interval reported above lasted, in these conditions, a few hours. In order to obtain reproducible results, an electrochemical surface cleaning stage consisting in the 0 V vs SCE polarization of the WO_3 electrode for 30 s was introduced after each single point EIS experiment during the scanning of the potential interval reported above. EIS data were fitted to equivalent RC circuits by using Z-View (Scribner). All photoelectrochemical measurements were carried out in front (electrolyte side) illumination.

Oxygen evolution measurements in various electrolytes under photoelectrolytic conditions were carried out in a sealed electrochemical cell under potentiostatic conditions at 1.5 V vs SCE by using a Crison Oxy 45+ amperometric oxygen probe (model 51 20) calibrated in wet air. The blank, i.e. the maximum concentration of dissolved oxygen that, due to seal imperfections, was detected in the dark at the end of a time interval equivalent to that of the photoelectrolysis (typically 60-120 minutes), was subtracted in order to estimate the faradic yield according to the Faraday's laws.

EPR and fluorescence spectroscopy. EPR spin-trapping experiments were carried out with a Bruker MRD spectrometer equipped with a TE 201 resonator (microwave frequency of 9.4 GHz). The samples were suspensions of WO_3, obtained by calcination of the same colloid precursor used for film fabrication, in aqueous solutions containing H_2SO_4 (0.1 M) and α-phenyl N-tert-butyl nitrone (pbn, 5 x 10^{-2} M) as spin trap. When requested $TBAHSO_4$ (0.1 M) was used instead of H_2SO_4. The samples were put into a flat quartz cell and directly irradiated ($\lambda > 420$ nm) in the EPR cavity with a medium pressure mercury lamp. No EPR signals were obtained in the dark and during irradiation of the solution in the absence of WO_3. Other experiments were carried out by suspending WO_3 in 0.1 M H_2SO_4 containing either 0.1 M or 20% v/v methanol. Both pbn and DMPO were used as spin traps in parallel experiments.

Photochemical experiments for ·OH detection based on the hydroxylation of coumarin were carried out irradiating ($\lambda > 420$ nm, 30') aqueous suspensions of WO_3 containing H_2SO_4 or $TBAHSO_4$ (0.1 M) and coumarin (1 x 10^{-4} M). After irradiation and centrifugation the fluorescence spectrum (λ_{exc}= 332 nm) of 7-hydroxycoumarin, possibly formed, was recorded at room

temperature with a Jobin Yvon Spex Fluoromax II spectrofluorimeter equipped with a Hamamatsu R3896 photomultiplier. Both emission and excitation slits were set at 3 nm during these measurements.

Transient Absorption Spectroscopy and Spectroelectrochemistry. TAS spectra were obtained on transparent WO_3 electrodes under applied positive potential (vs SCE) by using a previously described spectrometric apparatus,[33] based on the third harmonic (355 nm) of a Nd:YAG laser as nanosecond (FWHM ca. 7 ns) excitation source. Briefly, the laser light was attenuated to ca. 4 mJ/cm^2 by defocusing the beam with a plano concave lens while the probe light generated by a Xe lamp was attenuated with a 25 % T and a 0.3 A neutral density filters. A combination of 532 nm notch filter and of 380 and 420 nm cut offs prevented scattered laser light to reach the photomultiplier. The electrode was inserted into a cell made of optical glass having flat walls fitting in the cell holder of the spectrometer. The film was oriented with a goniometric holder with respect to both the excitation and probe beams in order to maximize the amplitude of the oscilloscope traces, their relative S/N ratio and to improve the reproducibility of the excitation and probe geometry when reassembling the cell to explore other electrodes or electrolytes. The complete decay of the transient signals spanned a 10^{-9}-10^{-1} s range, thus decays in the 10^{-4}-10^{-1} s interval were acquired by disabling the pulsing unit and by amplifying through a 1 MΩ oscilloscope input impedance and averaging over hundreds laser shots having a maximum repetition rate of 1 Hz.

Spectroelectrochemical data under slightly negative polarization (-20 and -50 mV vs SCE) were acquired by using the previously described cell and electrode configuration inserted in an Agilent Technologies Cary 300 UV-Vis spectrophotometer. Difference absorption spectra were obtained by subtracting the spectral contribution of the same film immersed in the electrolyte prior to polarization (disconnected wires).

WO_3 electrode preparation: WO_3 films on tungsten foils (Type A electrodes) were prepared by accelerated potentiostatic anodization applying 40 V at 40 °C for 7 hours in the presence of an electrolyte consisting of NMF/water 8/2 + 0.05% NH_4F followed by 550 °C annealing for 1 hour as described in previous contributions[34, 35], resulting in a porous oxide layer ca. 2 μm thick. Transparent nanocrystalline electrodes (Type C electrodes) cast onto well cleaned FTO glass were prepared by spin coating (PiChem Model KW-4A spin coater, spinning 6 s at 500 rpm followed by 20 s at 2000 rpm) an aqueous colloidal precursor densified with carbowax (15000-20000 u, Aldrich) as organic binder[13]. Briefly, up to six spin coated layers were sequentially deposited, each layer being thermally annealed at 550 °C for 30 minutes in air before deposition of the following layer yielding electrodes having a thickness of ca. 1.5 micron, estimated by SEM imaging (Figure

S1). Prior to photoelectrochemical measurements the electrodes were activated by soaking in 1M H_2SO_4 for two hours, followed by a final treatment at 550 °C for 45 minutes.

Results and Discussion

1. *Electrode Morphology and DC Photoelectrochemistry*

This study originated from the observation[36] of enhanced photocurrent generated by anodic WO_3 substrates when illuminated in electrolytes containing tetrabutyl-ammonium salts which, in our opinion, deserved a deeper understanding. In order to confirm and extend such observations, improved transparent colloidal electrodes with a photoanodic response equal or superior to that of anodic substrates were prepared. Substrates obtained with 6 sequential spin coating runs showed maximum IPCE exceeding 60 % and a relatively broad photoconversion spectrum extending up to 470 nm (Figure 1C). The development of efficient colloidal transparent electrodes was considered a pre-requisite to a meaningful TAS investigation, where the charge transfer dynamics of photoelectrodes characterized by high photon to electron conversion yields could be in principle extended to other substrates characterized by similar performances, albeit with possibly different morphologies or optical properties. The AFM imaging of the colloidal WO_3 substrate after 1 (Figure 1 A) and 6 spin coating runs (Figure 1B) reveals the presence of well sintered roughly spherical nanoparticles of average diameter of ca. 70 nm. The presence of voids and valleys at least 100 nm deep is evident in the film obtained after a single deposition, but these features disappear after multiple depositions, leaving a homogeneously covered surface with maximum height differences which roughly correspond to the diameter of a single nanoparticle. The more complete and homogeneous surface coverage by WO_3 nanoparticles, the thickening of the photoactive layer and the concomitant increase in light harvesting explains the progressive broadening of the action spectrum and the shift of the photoconversion onset toward the red. The performances clearly tend to become asymptotic after the 5-6th deposition, which were therefore deemed satisfactory to our purposes.

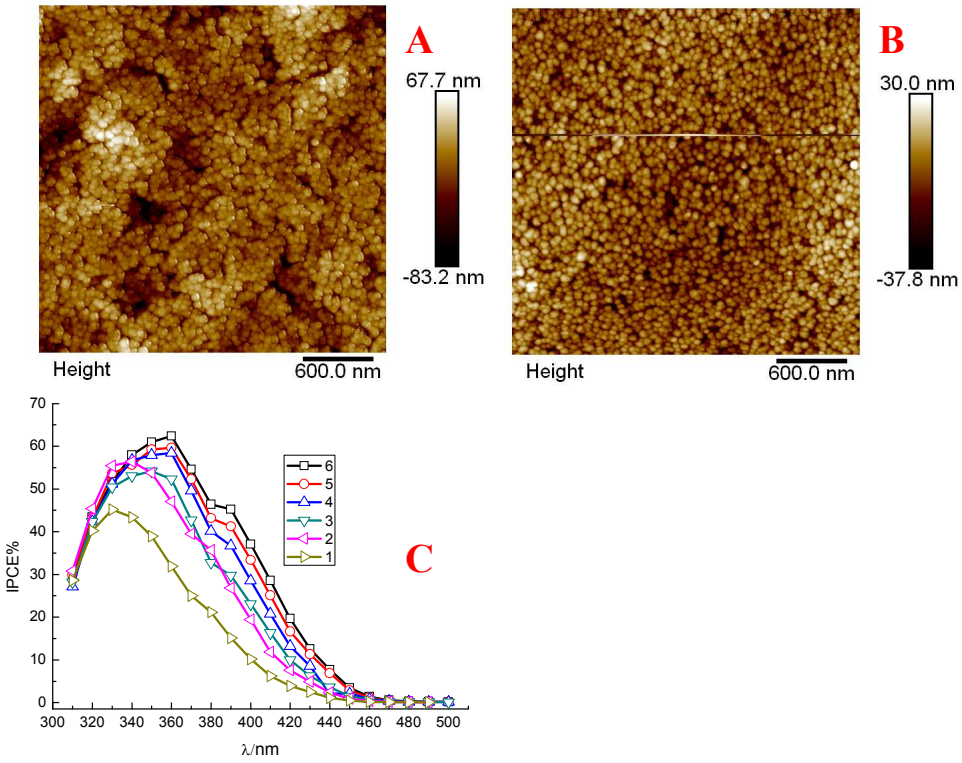

Figure 1. AFM images of transparent WO_3 electrodes obtained after the first (A) and after the sixth (B) spin coating deposition of colloidal precursor and the photoelectrode trend in monochromatic photoconversion efficiency (C) in 0.1 M H_2SO_4 at 1.5 V vs SCE.

By contrast, the anodically grown electrodes in NMF electrolytes show a porous morphology consistent with earlier reports,[17] showing a corrugated oxide surface with winding structures, resembling ridges, crests and valleys which can be considerably deep, of the order of hundreds nanometers (Figure 2A). Higher resolution 3-dimensional analysis (Figure 2B) clearly show the crests to be consisting of fused roughly spherical substructures having diameters of 80-100 nm. The absorption spectra of the different WO_3 films reveal a light harvesting efficiency higher than 90 % in the near UV region ($\lambda \leq 390$ nm), with the optical absorption extending into the visible region, up to 450-460 nm (Figure S2).

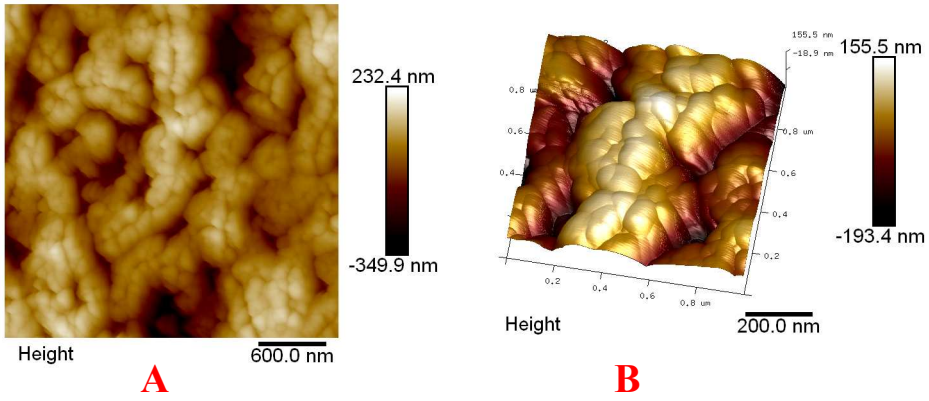

Figure 2. (A) AFM images of anodically grown WO_3 films (scanned area 3x3 μm) and higher resolution (1μm^2) 3D topographic picture of a ridge structure (B).

The performances of the 6-layer colloidal electrodes (type C Figure 3 (1)) rival those of the anodic electrodes (type A Figure 3(1)) in 0.1 M H_2SO_4, where similar currents, of the order of 1.5 mA/cm^2 at 1.5 V vs SCE are observed under 1 sun illumination. The JV characteristic of the colloidal electrode is steeper than that of the anodically grown WO_3, which, however, differently from the colloidal one, does not show a clear photoanodic plateau starting from 1 V vs SCE, but a slowly rising photocurrent as the voltage is progressively moved to more positive values. The response of both electrode types is considerably increased in 0.1 M $TBAHSO_4$ (pH 2.5), showing an anticipated photoanodic onset of ca. 100 mV and limiting photocurrents ≥ 2 mA/cm^2, 35-40% higher than those measured in sulfuric acid. Correspondingly, maximum IPCEs ≥ 70 % (Figure 3 (2)) were measured. It can be appreciated that the maximum IPCE generated by type C electrodes in the presence of TBA^+ exceeds 80 % in the UV region, whereas the anodically grown substrates display lower maximum values accompanied by a better responsivity to longer λ (from 420 nm onwards), probably due to improved harvesting of the more penetrating photons scattered and trapped within the opaque porous film. Nevertheless their lower maximum IPCE suggests a slightly lower capability of type A electrodes to collect the charge carriers generated in the 410-390 nm interval. Out of several HSO_4^- based electrolytes, containing counter cations of different sizes, (H^+ Li^+, Na^+, K^+, NH_4^+) the photoanodic enhancement was observed with both electrode types exclusively in the presence of alkyl-ammonium cations (TBA^+ and TMA^+) generating nearly identical performances (Figure S3) and evidencing that the mechanism of charge separation,

originating both higher photocurrents and anticipated photoanodic threshold, must be specific to the chemical nature of these organic species and probably irrespective of their size.

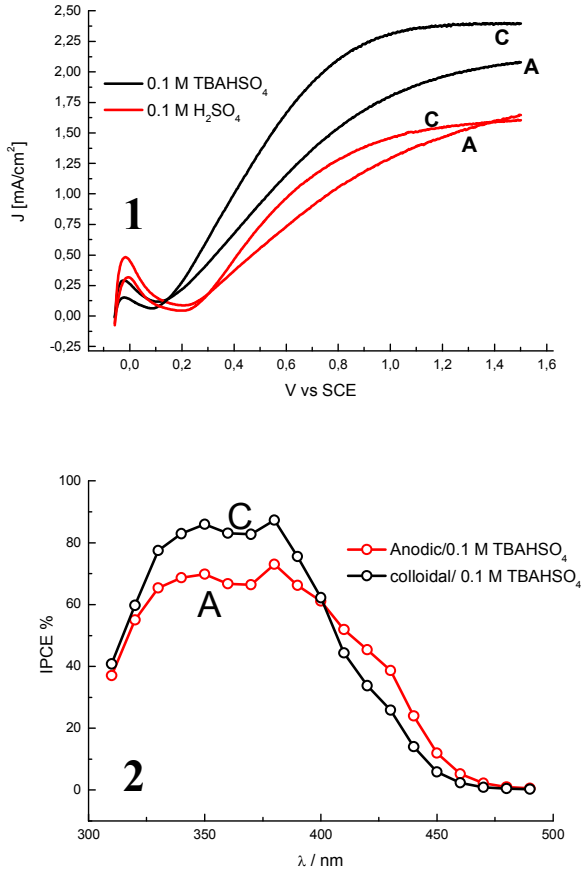

Figure 3. (1) JV curves under 1 sun illumination of type A and C electrodes in the presence of 0.1 M H_2SO_4 (red) and of $TBAHSO_4$ (black). (2) IPCE of type (A) (red) and type (C) (Black) in 0.1 M $TBAHSO_4$ at 1.5 V vs SCE.

Photocurrent transients (Figure S4) under simulated sunlight, showed that the charge transport across the WO_3 film was significantly influenced by the anodic bias, as, at increasingly positive polarization, steeper photocurrent rise and faster decay were observed when light was chopped on and off respectively, consistent with a faster movement of photogenerated electrons towards the electron collector and with a concomitant injection of holes into the electrolyte. Different dynamic processes, including diffusion, drift and recombination of charge carriers affect the shape and the temporal decay of the transients, therefore FWHMs have here only a qualitative and comparative meaning. Nearly identical peak FWHMs, on the order of 3-5 10^{-2} s, were found in both anodic and colloidal films in 0.1 M H_2SO_4 (Table 1), indicating, once more, the similarity of these substrates with respect to their charge separation and charge transport characteristics. Despite the larger size and expected lower mobility of TBA^+ with respect to H^+ and Li^+, the electrolyte composition had

a quite minor influence on the FWHM and was found only marginally higher in the case of $TBAHSO_4$, particularly at bias > 0.8 V vs SCE, where the photocurrent is significant (Table 1). Since, in a porous electrode, the movement of cations of the electrolyte should electrostatically compensate the motion of the negative charge left inside the WO_3 film, once hole scavenging has occurred, we can conclude that either the differences in ionic mobility (which should also consider interactions of the positive ions with the WO_3 surface) are not so large to significantly modify the charge transport across WO_3 films ≤ 2 μm thick, or that protons, arising from the dissociation of $(HSO_4)^-$ play the major role as charge compensating cations, leading to similar results in all $(HSO_4)^-$ based electrolytes. Nevertheless, the charge transport properties evaluated in the presence of TBA^+, being inferior or at best equal to those found in the presence of a larger concentration (0.1 M) of smaller cations like H^+ and Li^+, cannot explain the improved photoanodic response observed in TBA and TMA electrolytes.

Table 1. FWHM obtained from photocurrent transients under anodic bias in 0.1 M HSO_4^- based electrolytes. (A) Anodic WO_3; (C) Colloidal WO_3

Bias (V vs SCE)	$FWHM^{(A)}$ (s) (H_2SO_4)	$FWHM^{(C)}$ (s) (H_2SO_4)	$FWHM^{(C)}$ (s) ($TBAHSO_4$)	$FWHM^{(C)}$ (s) ($LiHSO_4$)
0.3	0.057	0.057	0.118	0.053
0.6	0.047	0.048	0.063	0.047
0.8	0.044	0.046	0.058	0.044
1	0.041	0.042	0.051	0.041
1.2	0.039	0.040	0.047	0.039

Voltammetric curves of Type A WO_3 acquired in the dark at strong anodic potentials (Figure S5) did not reveal any anticipated anodic onset in the TBA containing electrolyte with respect to simple H_2SO_4. Both electrolytes show a dark anodic onset > 2.5 V vs SCE, with the $TBAHSO_4$ onset (≈ 2.7 V vs SCE) > H_2SO_4 (≈2.5 V), values generally consistent with the expected WO_3 valence band edge position, allowing to rule out the direct participation of TBA^+ to hole scavenging processes, or at least to those directly originating from the top of the valence band. It should be noted that the anodically grown substrates were used for these experiments because the complete coverage of the ohmic collector by a passive oxide layer should prevent direct electrolyte discharge at the back

contact. This process would probably occur with colloidal electrodes, where the electrolyte can reach the FTO surface through film porosities.

The performance enhancing role of TBA is masked, or becomes immaterial, in the presence of a large excess of a known hole scavenger for WO_3. Indeed, the addition of methanol (20% v/v) to both H_2SO_4 and $TBAHSO_4$ results in a levelling of the WO_3 performances in the two different electrolytes, in both of which the limiting photocurrent reaches ca. 3.5 mA/cm^2 at ca. 1V vs SCE (Figure 4). Reduced electron/hole recombination and secondary electron injection[5] by strongly reducing methanol radical species (≈ - 1 V vs SCE) formed in the photooxidation process explain the more than doubled current with respect to pure H_2SO_4.

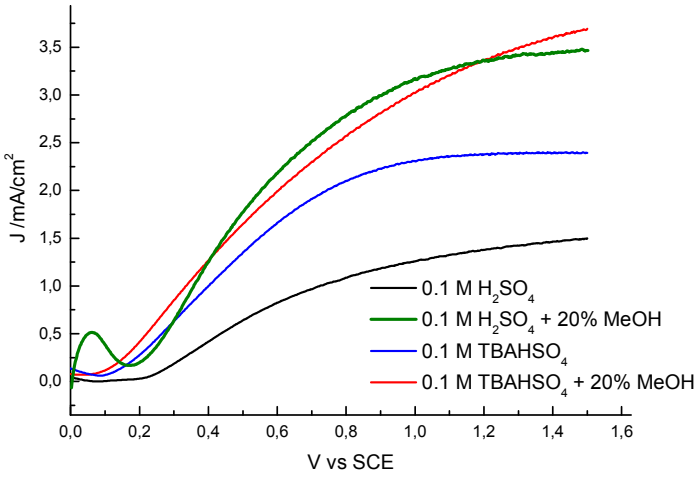

Figure 4. JV curves of colloidal WO_3 films in the presence of various electrolytes under 1 sun simulated illumination: (0.1 M H_2SO_4, black); 0.1 M $TBAHSO_4$ (blue); 0.1 M TBAHSO + 20 % (v/v) methanol (red); 0.1 M H_2SO_4 + 20 % (v/v) methanol (green).

Detection of oxygen photoproduction in solution during a photoelectrolysis process of the duration of at least one hour at +1.5 V vs SCE (Figure 5), reveal that molecular oxygen is found in the presence of Li^+, H^+ and NH_4^+, with a faradic yield in the order of 10-15 % (11 % and 12 % for sulphuric acid and $LiHSO_4$, 16 % for NH_4HSO_4) but is nearly 0 in the presence of both TBA^+ and TMA^+. When photoelectrolysis of the $TBAHSO_4$ electrolyte is carried out in an air saturated solution contained in a nitrogen pressurized sealed cell, oxygen is actually consumed (Inset Figure 5 upside down triangles), declining progressively from ca. 7 mg/l to ca. 3 mg/l in about 30 minutes. A similar behaviour is reported in the presence of H_2SO_4/methanol where oxygen consumption is even faster, dropping to ca. 1 mg/l in ca. 60 minutes (Inset Figure 5, circles). These observations are consistent with the production of hydroxyl radicals as one of the primary water oxidation products (1), which are able to extract hydrogen atoms from the alkyl chains of the alkyl-ammonium salts (R,

in (2)), forming organic radicals which could be less reactive with respect to electron recombination at the WO_3 surface or that quickly undergo a further reaction with water, forming secondary alcohols (3), or with dissolved oxygen to form peroxides (3'), explaining the progressive disappearance of oxygen

$h^+ (WO)_3 + H_2O \rightarrow \cdot OH + H^+$ (1)

$\cdot OH + R \rightarrow R\cdot + H_2O$ (2)

$R\cdot + H_2O \rightarrow ROH + \cdot H$ (3)

$R\cdot + O_2 \rightarrow ROO\cdot$ (3')

$ROO\cdot + H\cdot \rightarrow ROOH$ (4)

$\cdot OH + H\cdot \rightarrow H_2O$ (5)

$R\cdot + \cdot R \rightarrow R_2$ (6)

Scheme 1. Chemical reactions following formation of ·OH at the WO_3 interface in the presence of an organic species R containing alkyl chains. (3) and (3') are possible oxidation reactions involving R· as secondary oxidation intermediates, (4) (5) and (6) represent possible radical recombination pathways.

Clearly, all these organic intermediates resulting from hydrogen extraction can undergo further subsequent direct or ·OH mediated oxidations. A similar oxidation pathway is feasible for methanol, which, besides participating to direct oxidation with holes at the WO_3 surface, is prone to secondary scavenging of ·OH to form hydroxy-methylene radicals ($\cdot CH_2OH$) also susceptible of reaction with molecular oxygen. The final results is, in any case, an improved photoanodic response of the WO_3 electrodes, due to decreased interfacial recombination, which explains both the anticipated photoanodic onset and increased limiting photocurrent observed in the presence of alkyl-ammonium salts.

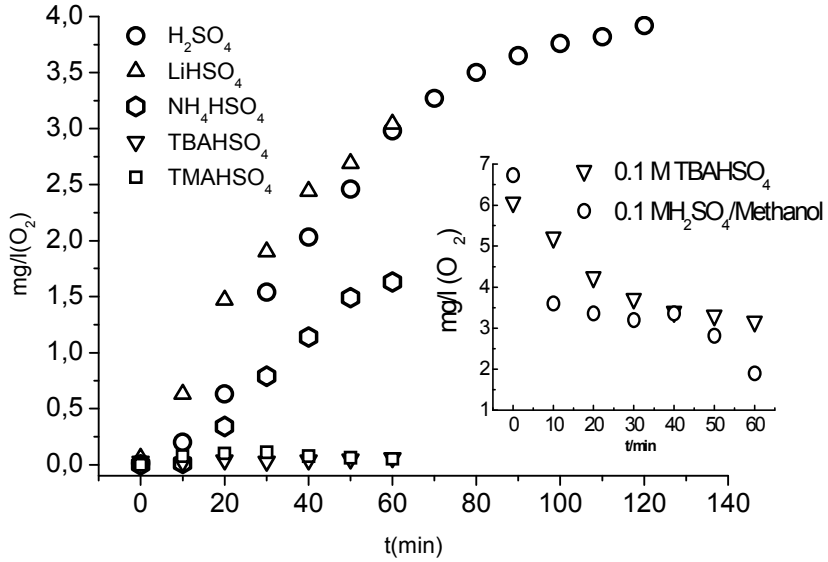

Figure 5. Production of oxygen during constant potential (1.5 V vs SCE) photoelectrolysis in different electrolytes: 0.1 M H_2SO_4 (circles); 0.1 M $LiHSO_4$ (triangles); 0.1 M NH_4HSO_4 (diamonds); $TBAHSO_4$ (upside-down triangles); $TMAHSO_4$ (squares). Inset: variation of the O_2 concentration during the photoelectrolysis of initially air saturated solutions containing 0.1 M $TBAHSO_4$ (upside-down triangles) and 0.1 M H_2SO_4 + 20 % (v/v) MeOH (circles).

·OH intermediates may therefore constitute active recombination centres, by reacting with photogenerated electrons at the semiconductor surface, reconstituting in acidic environment the water molecule (7), or forming H_2O_2, which, in turn, can be further oxidized to molecular oxygen (9), or act as electron scavenger at the semiconductor surface. Finally, hydroxyl radicals can extract hydrogen from HSO_4^- resulting in the formation of $SO_4^{\cdot-}$ which couple to form $S_2O_8^{2-}$ (10).

$$\cdot OH + e^- (WO_3) + H^+ \rightarrow H_2O \quad (7)$$

$$2 \cdot OH \rightarrow H_2O_2 \quad (8)$$

$$H_2O_2 + 2\, h^+ (WO_3) \rightarrow O_2 + 2H^+ \quad (9)$$

$$2 \cdot OH + 2\, HSO_4^- \rightarrow 2\, H_2O + S_2O_8^{2-} \quad (10)$$

Scheme 2. Reactions involving ·OH electrolytes in the presence of HSO_4^- anions

Both H_2O_2 and $S_2O_8^{2-}$ are known oxidation byproducts of photoelectrolytic processes involving WO_3.[30, 37] The number of side reactions in which ·OH intermediates can be involved, only a few of which actually leading to the formation of molecular oxygen, can explain the relatively low faradic yield for O_2 evolution found in this study (although we measured only the photoproduced

oxygen dissolved in solution and not that collected in the head space of the cell) and are quite consistent with observations by Mi et. al.[30] in sulphate containing electrolytes. Further, in the presence of many organic species undergoing hydrogen extraction by hydroxyl radicals, like methanol or alkyl ammonium salts herein considered, the activation of an additional ·OH scavenging pathway should suppress almost completely oxygen production via formation and subsequent oxidation/decomposition of H_2O_2.

The generation of ·OH radicals in WO_3 aqueous suspensions under visible light illumination ($\lambda > 420$ nm) was confirmed by EPR spin trapping measurements, where the nature of the trapped radical can be identified by the parameters obtainable from the EPR spectrum. Few seconds photoirradiation of the WO_3 suspension in the presence of pbn causes the prompt formation of a triplet of doublets (a_N = 15.4 G, a_H = 2.7 G), which is shown in Figure S6. Coupling constants values are in agreement with the trapping of ·OH by pbn to form the paramagnetic adduct [pbn-OH]·.[38] Moreover, if the experiment is carried out with DMPO as spin trap, the typical quartet (1:2:2:1, $a_N = a_H$ = 14.8 G) is obtained immediately after light is switched on, further confirming the formation of OH radicals.[39] Control experiments show that no signal is observed neither in the dark nor during irradiation in the absence of WO_3. These results confirm that photoexcited WO_3 is able to initiate water oxidation by producing OH radicals, corroborating the previous hypothesis.

The generation of OH radicals by WO_3 was also confirmed by observing the emission of 7-hydroxycoumarin, following a method already validated for revealing hydroxyl radicals produced by photoexcitation of TiO_2.[40] Upon reaction with hydroxyl radicals, coumarin produces 7-hydroxycoumarin, originating, under UV excitation, a characteristic emission peaking in the blue at ca. 470 nm (Figure 6 A).

When WO_3 is irradiated in aqueous solutions containing $TBAHSO_4$ (0.1 M) and pbn ($5x10^{-2}$ M) the triplet of doublets ascribed to [pbn-OH]· is revealed again, but its intensity is lower than in the previous case (Figure S7), suggesting the presence of an additional ·OH scavenging pathway. In line with this result, Figure 6 curve (c) shows that irradiation of WO_3 in the presence of $TBAHSO_4$ does not accumulate fluorescent 7-hydroxy coumarin. Moreover, in $TBAHSO_4$ the formation of new radical species trapped by pbn and partially overlapping with [pbn-OH]· is actually observed by EPR at longer irradiation time, with coupling constants (a_N=16.0 G, a_H= 4.3 G) diagnostic of the trapping of carbon centered radical[38] (Figure S8), ostensibly generated by hydrogen abstraction from alkyl chains of TBA. Irradiation of WO_3 in the presence of 0.1 M methanol leads to the formation and trapping of OH radicals but no organic radicals coming from methanol, are trapped and detected under our experimental conditions. When WO_3 is suspended in the presence of a large amount of methanol (20% MeOH in 0.1 M H_2SO_4) no paramagnetic signal is revealed at all. The

formation of OH radicals is apparently suppressed but, at the same time, radicals of methanol are not efficiently trapped. These results suggest that methanol can be either directly oxidized by the photogenerated holes without the mediation of ·OH or that MeOH radicals resulting from the quantitative scavenging of ·OH are efficiently consumed, for example by charge injection into WO_3, before being captured by the spin trap. Hole transfer kinetics, observed by TAS as well as EIS results (see sections 2 and 3) support the predominance of the second mechanism over the former.

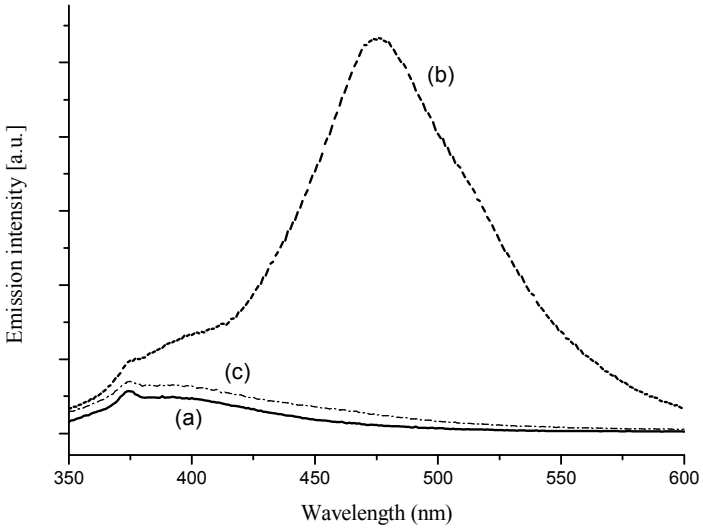

Figure 6. Emission spectra upon 335 nm excitation: (a) WO_3 suspended in water containing H_2SO_4 (0.1 M) and coumarin (1 x 10^{-4} M) before irradiation, (b) sample (a) after 30' irradiation ($\lambda > 420$ nm), (c) WO_3 suspended in water containing $TBAHSO_4$ (0.1 M) and coumarin (1 x 10^{-4} M) after 30' irradiation ($\lambda > 420$ nm).

2. Photoelectrochemical Impedance Spectroscopy

The observation of ·OH production from WO_3 substrates under illumination indicates that the hole transfer should occur via valence band or via very deep trap surface states, otherwise the thermodynamics would be unfavourable to OH radical generation. A DFT investigation[41] of oxygen evolution on monoclinc WO_3 pointed out that, also thanks to the stabilizing surface interactions of the OH· intermediate with the semiconductor surface, the first monoelectronic oxidation of water, possibly finally leading to O_2 evolution, should be thermodynamically viable at a potential of 2.3 V vs NHE, much lower than the valence band edge of WO_3 at ca. 2.8-2.9 V vs NHE.

Impedance Spectroscopy under photocurrent generation conditions may help to shine light on the photocurrent generation mechanism in WO_3 through the resolution in the frequency domain

of the faradic processes. Complex plane (Nyquist) plots of WO_3 under illumination show two depressed semicircles, one very small at high frequency and one, having a much larger diameter, at lower frequencies, as schematized, for sake of clarity, in Figure 7. The complex plane plots obtained from the real experiment at a representative voltage (0.35 V vs SCE) are reported in Figures S9 and S10. Clearly, the projection of the large low frequency semicircle on the real axis accounts for the large majority of the total photoelectrode resistance. The resistance of the low frequency arc is quantitatively well correlated, through its inverse, with the derivative of the i-V characteristics (Figure S11), indicating its origin in the dynamic processes that control photocurrent generation and was thus assigned to the hole transfer resistance (R_{hT}) from WO_3 to the electrolyte. The higher frequency semicircle (HF arc) was characterized by an associated resistance that was substantially independent on the voltage and could be attributed to geometric factors[42] (i.e. porosity of the photoelectrode) or to passive interfaces having an high frequency capacitive response (WO_3/FTO or WO_3/W interfaces in either type C or type A electrodes). Clearly type A and type C photoelectrodes had a qualitatively identical response to the small amplitude AC perturbation and the same equivalent circuit (Figure 7), consisting of two serial RC parallel meshes, was used to fit the experimental results where the two parallel RC (where C = Constant Phase Element (CPE) accounts for the non ideality of the electrochemical capacitances) describe the high frequency arc and the charge transfer arc respectively.

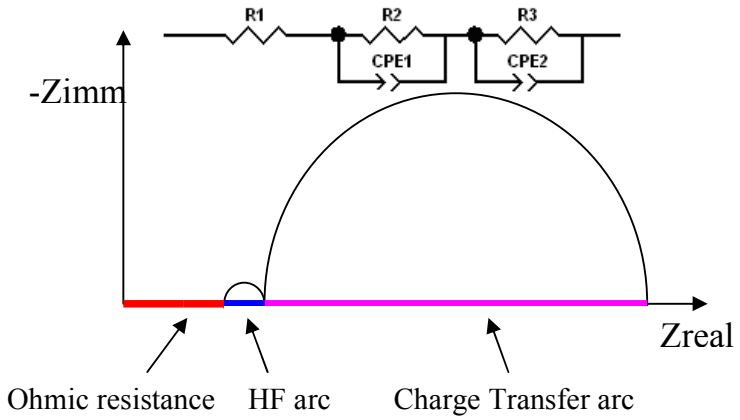

Figure 7. Schematization of typical impedance response, in the form of Nyquist plots, of WO_3 photoelectrodes under photocurrent generation conditions and equivalent circuit used for the fit of the experimental data.

The low frequency capacitance associated with the charge transfer arc has often a diagnostic importance for determining the mechanism of interfacial charge transfer. When surface states are involved, a bell shaped distribution should be observed, corresponding to variations of chemical capacitance due to progressive filling/emptying of these states[43]. When the charge transfer occurs through the valence band and the voltage drop involves the space charge layer of the semiconductor, the photocurrent is the result of potential-induced variations of hole density at the surface of the material. In the case of both WO_3 substrates used in this study (A and C), the low frequency capacitance associated with the charge transfer resistance was found to follow convincingly the Mott-Schottky (M-S) behaviour, resulting in linear $1/C^2$ vs voltage plots (Figure 8 (1) and (2)) suggesting that hole transfer proceeds through the valence band. The slopes of the n-type M-S plots provide donor densities (Table 2)) in general good agreement with values reported in the literature for monoclinic WO_3, spanning a typical interval from 1×10^{20} to 1.5×10^{21} cm^{-3} depending on the oxide preparation route and conditions.[35, 44] Colloidal electrodes (C) are characterized by donor densities ($Nd_{average} = (1.2 \pm 0.2) \times 10^{20}$ cm^{-3}) which are ca. 6 times lower than those found for the anodic substrate (A) ($Nd_{average} = (6.5 \pm 1.5)\times 10^{20}$ cm^{-3}). The majority carrier density found in our colloidal substrates approaches the optimal values recently reported by

Zhao et. al.[45] for similar types of nanostructured WO_3 electrodes which were subjected to electrochemical doping at moderately negative potentials, suggesting the possibility that the electrochemical conditioning stage at 0 V vs SCE , adopted in this study prior to each potentiostatic or potentiodynamic experiment, also contributes to tune the carrier density, enhancing the photoanodic response by increasing WO_3 film conductivity and by controlling the depletion length. Indeed, the M-S intercept yields, in all cases, flat band potentials which agree with the positive photoanodic onset observed from the i-V characteristics of both electrode types in the different electrolytes. It can be further observed that the flat band potentials found for the anodic substrates are more negative by ca. 60 mV than those found for the colloidal electrodes in identical conditions. The introduction of an excess of methanol as hole scavenger does not alter the behaviour reproduced in the aqueous electrolytes containing different cations (H^+, Li^+, TBA^+) indicating that the charge separation mechanism, even in the presence of hole scavengers of known activity, remains essentially unchanged.

The length of the depletion layer (L_{dl}), where the electric field is active in directing the minority carriers (photoholes) to the interface with the electrolyte, is given by equation (11), which is obtained from the simplest form of Poisson equation (planar electrode, constant donor density) having thus only an approximate meaning in our case, which is nevertheless useful for understanding the different JV characteristics of colloidal and anodic WO_3 substrates.

$$L_{dl} = \sqrt{\frac{(2\varepsilon\varepsilon_0)(E - Efb - kT/e)}{(Nde)}} \quad (11)$$

In equation (11) the term *(E-Efb-kT/e)* can be regarded as the potential drop occurring within the space charge, with an approximation of 26 mV at 298 K. With the flat band potentials found in our case, this term becomes approximately equal to 1 V at a potential of 1.2-1.3 V vs SCE at which the photocurrent generated by colloidal substrates usually reaches saturation. In the presence of such bias, with the doping levels found for type C electrodes, the space charge region should extend into the nanostructures for a length which becomes comparable to their radius (30-40 nm), therefore the field assisted charge extraction should reach its maximum efficiency and no significant photocurrent gains are observed by further increasing the voltage to more positive values. The depletion layer should have a much shorter absolute extension (5-6 nm) in the case of the anodic substrates, due to their average donor density ca. 6 times higher than the colloidal substrates. Moreover, the anodic substrates are characterized by the presence of larger sintered nanostructures

having a radius of ca. 50 nm, in which the charge carriers may have to diffuse in a field free regime over a longer distance before reaching the depletion region. This contributes to explain several comparative observations reported in this study: 1) the lower maximum collection efficiencies (lower maximum IPCEs) of the anodic substrates with respect to the multilayered colloidal films developed for this work; 2) the smoother slope of the i-V characteristics of type A electrodes, originated by a narrower depletion region which slowly develops inwards as the potentials moves towards positive values, progressively increasing the charge collection efficiency 3) the absence of a clear photocurrent saturation region at potentials at which the colloidal substrates already show a distinct limiting current, due to the fact that, at these voltages, the depletion length in the anodic film is still much smaller than the average radius of the composing nanostructures.

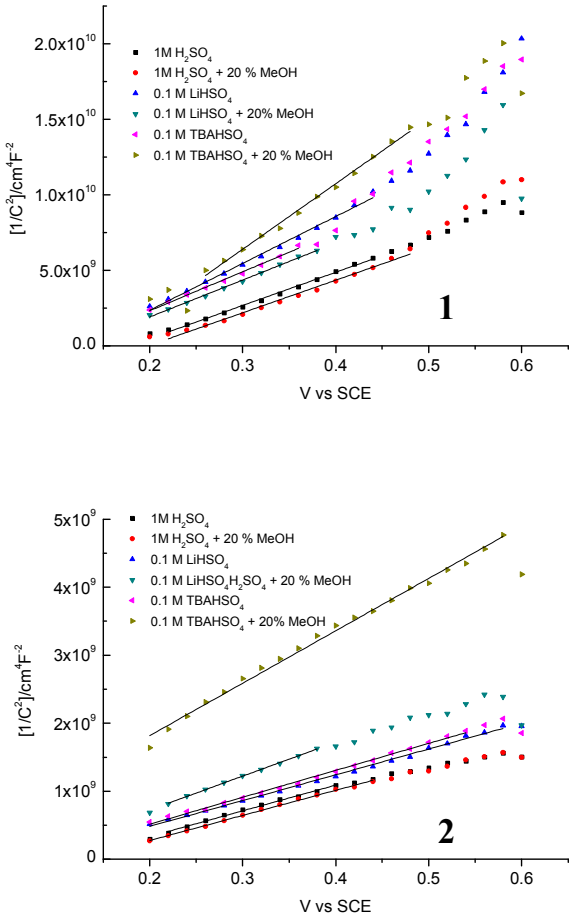

Figure 8. Mott-Schottky plots representing $1/C^2$ vs voltage for the type C (1) and type A (2) WO_3 electrodes under solar illumination in the presence of different electrolytes containing H_2SO_4, $LiHSO_4$ and $TBAHSO_4$ either in the absence or in the presence of Methanol as hole scavenger. C represents the low frequency capacitance calculated from the CPE admittance (Y) and ω_{max} (angular frequency of the arc maximum) according to $C = Y(\omega_{max})^{n-1}$ where n is the CPE exponent extracted from the fit.

Table 2. Donor Densities (Nd) and flat band potentials (Efb) extracted from M-S plots for colloidal (C) and anodic (A) electrodes

Electrolyte	Nd (10^{20} cm^{-3}) (C)	Nd (10^{20} cm^{-3}) (A)	Efb (V) (C)	Efb (V) (A)
1M H_2SO_4	1.3	7.5	0.21	0.15
1M H_2SO_4 + 20 % MeOH	1.3	7.6	0.24	0.17
0.1M $LiHSO_4$	0.9	7.4	0.16	0.11
0.1M $LiHSO_4$ + 20% MeOH	1.2	5.7	0.16	0.09
0.1M $TBAHSO_4$	1.1	7.1	0.15	0.11
0.1M $TBAHSO_4$ + 20% MeOH	0.7	3.7	0.19	0.04

3 Transient Absorption Spectroscopy

Transient Absorption Spectroscopy (TAS) was employed to directly address the fate of holes photogenerated into WO_3 by exploring the effect of different electrolytes compositions and of the applied potential on the lifetime of the minority charge carriers. To the best of our knowledge only few TAS studies on transparent WO_3 films under photocurrent generation conditions can be found in the literature and are all relatively recent. Pesci et al.[46] employed TAS to identify the spectral signatures of photoholes at open circuit in the presence of Ag^+ as electrons scavenger. Kim et al.[47] used TAS to investigate recombination events in SiO_x modified WO_3 films under electrochemical polarization, but the temporal window was limited to just several microseconds, enough to appreciate differences in electron-hole recombination, but not for framing the complete decay of the spectral signatures of the charge carriers. In agreement with these previous studies, and with steady state spectroelectrochemical data under negative polarization (Figure S12), we were able to assign the intense absorption in the blue 430-460 nm (Figure 9 (1)), observed upon 355 nm excitation, to photoholes, while electrons contribute to the absorption at longer wavelengths. The amplitude of the 430 nm absorption maximum increases exponentially with the applied potential (Figure S13), a behaviour which should reflect the presence of the depletion layer, where the concentration of the photogenerated minority carriers p^*_S at the surface should vary according to $p^*_s = p^*_{bulk} exp(eV/kT)$ where $V=(E-Efb)$ is the potential drop occurring within the space charge

layer. The long lived component of the decay (for $t > 10^{-4}$ s), which is relevant to the description of the heterogeneous hole transfer kinetics, is due to both direct and mediated electron/hole recombination *(k_{rec})* and charge transfer to the electrolyte and could be well fitted with monoexponential functions, suggesting, as a first approximation, a pseudo-first order kinetic model of the type

$$-\frac{dp^*_s}{dt} = (k_{rec} + k_{hT} + k_{scavenger})\, p^*_s \quad (12)$$

where the lifetime τ is defined by $\tau = \frac{1}{k_{rec} + k_{hT} + k_{scavenger}}$ in which the hole transfer rate constant to water k_{hT} has been separated from that originated by direct reaction of the hole with the sacrificial electron donor ($k_{scavenger}$) possibly present in solution. The decay in aqueous electrolytes was found to be nearly complete on a time scale of 0.05 s (Figure 9 (2)), in good agreement with the temporal width of the photocurrent transients under chopped illumination, corroborating the identity between the dynamic processes responsible for photocurrent generation and decay and the kinetics observed by TAS. Lifetimes of the order of 20 ms (H_2SO_4 and H_2SO_4 + 20% MeOH) and of 30 ms for $TBAHSO_4$ were obtained at 1.5 V vs SCE, confirming the role of $TBAHSO_4$ as secondary scavenger of OH radicals. In other words, in the presence of $TBAHSO_4$ k_{hT} involving the oxidation of water is unchanged, but the hole lifetime is increased due to a decreased k_{rec} involving ·OH as intermediate recombination centres. The presence of methanol resulted in a lifetime similar to that found for H_2SO_4, which may seem surprising, given the large improvement in photoanodic current observed in the presence of such scavenger. However, in this latter case the presence of an additional direct hole scavenging pathway having the rate constant $k_{scavenger}$ is probably offset by the decrease of k_{rec} since methanol can participate to the secondary scavenging of OH radicals as well. Comparative kinetics observed in $TBAHSO_4$ containing electrolytes based on different solvents (water, methanol, ethylene/propylene carbonate) show that the lifetime varies in the order water (≈30 ms) <methanol (≈ 100 ms) < ethylene/propylene carbonate (≈ 160 ms) (Figure 9 (3)). In these two organic solvents, where the production of OH radicals at the semiconductor surface should be largely absent (or just limited to the oxidation of water traces) the mediated recombination rate is reduced, resulting in significantly increased photohole lifetimes which are, however, also suggestive of relatively slow direct hole transfer to the electrolyte.

Current voltage curves in these purely organic electrolytes are indeed characterized by a resistive behaviour with very shallow slopes (Figure S14 (1)) which cannot be explained only by a decreased electrolyte conductivity, but also by a large increase in the charge transfer resistance, exceeding 500 Ohm, evidenced by EIS (Figure S14 (2)) and consistent with sluggish hole transfer

kinetics (R_{hT}(carbonates)>R_{hT}(MeOH)). Thus, based on these evidences, the improved photoanodic performances observed in the presence of sacrificial electron donors like methanol, is probably due to secondary reactions with OH radicals which firstly reduce the mediated recombination rate, followed, when thermodynamically allowed, by charge injection by the resulting organic radicals.

Finally, the lifetimes of the minority carriers were found substantially independent on the applied potential, in the whole potential interval where photoanodic current is observed (Figure 9(4)). This is consistent with the simple pseudo-first order kinetic model, where the potential dependence of p_s^* at both sides of equation (12) cancel out and with pseudo-first order rate constants which are largely potential-independent. This corroborates EIS results, pointing out that the applied potential predominantly drops within the space charge of the semiconductor and does not alter the activation energies for the interfacial charge transfer, but rather acts on the hole density at the semiconductor/electrolyte interface.

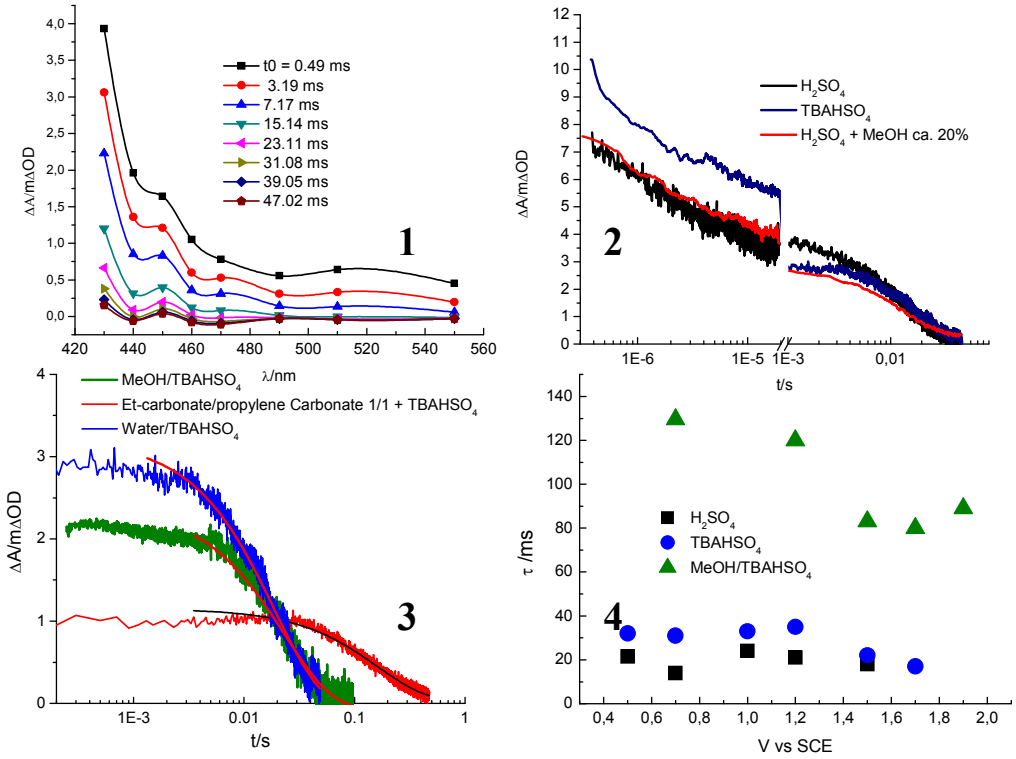

Figure 9. 1) Time evolution of the transient spectrum of colloidal WO_3 under 1.5 V vs SCE potential bias in 0.1 M $TBAHSO_4$ electrolyte; 2) 430 nm decay in aqueous electrolytes containing 0.1 M H_2SO_4 (black), 0.1 M $TBAHSO_4$ (blue); and 0.1 M H_2SO_4 + 20 % MeOH (red); 3) 430 nm decay in organic electrolytes compared to aqueous solvent in the presence of 0.1 M $TBAHSO_4$ at 1.5 V vs SCE: water (blue); methanol (green); ethylene-propylene carbonate 1/1 (red); 4) photohole lifetime as a function of the applied potential bias vs SCE in different electrolytes: 0.1 M $TBAHSO_4$ (blue); 0.1 M H_2SO_4 (black); MeOH/$TBAHSO_4$ (green).

Conclusions

The photoanodic response of two different types of nanocrystalline WO_3 electrodes prepared by following either the sol gel approach or the accelerated anodization route was studied in sulfate containing electrolytes with the aim of exploring the water oxidation intermediates and to outline the influence of the applied potential bias on the mechanism of charge separation at WO_3/electrolyte interfaces.

The evidences gained by combining potentiodynamic measurements, steady state photoelectrolysis, EPR and TAS indicate that OH radicals are among the primary oxidation intermediates, constituting, as a matter of fact, also active recombination centers. EIS indicates that the charge transfer occurs through the valence band and that the voltage drop mainly involves the space charge layer of the semiconductor, controlling the photocurrent via potential-induced variations of hole density at the surface of WO_3. Consistent with such indication the lifetimes of photoholes, measured by transient optical spectroscopy, were found substantially independent of the applied potential in the whole potential interval where photoanodic current is observed, confirming that the potential predominantly drops within the space charge of the semiconductor and does not alter the activation energies for the interfacial charge transfer.

Finally, this work suggests that WO_3 may find a successful application not only in photoelectrochemical cells for solar fuel production but should be considered also as a material for environmental photoremediation under visible light, promoting ·OH mediated oxidation reactions via valence band hole injection. Preliminary studies on the visible light photo-degradation of emerging organic contaminants of aqueous bodies, impervious to other decontamination techniques, have been successfully carried out in our laboratories and will be soon object of publication.

Acknowledgements

Financial Support from ENI (2012-2014) and from FIRB “Nanosolar” RBAP11C58Y are gratefully acknowledged.

Electronic Supplementary Informations available: Cross sectional SEM, photocurrent transients, JV curves in different electrolytes, EPR spectra, additional EIS and TAS data.

Notes and References

1. M. X. Tan, P. E. Laibnins, S. T. Nguyen, J. M. Kesselman, C. E. Stanton and N. S. Lewis, *Progress in Inorganic Chemistry* 1994, **41**, 21-144.
2. M. G. Walter, E. L. Warren, J. R. McKone, S. W. Boettcher, Q. Mi, E. A. Santori and N. S. Lewis, *Chemical Reviews*, 2010, **110**, 6446-6473.
3. A. Maldotti and A. Molinari, *Topics in Current Chemistry*, 2011, **303**, 185-216.
4. X. Chen and S. S. Mao, *Chemical Reviews*, 2007, **107**, 2891-2959.
5. B. D. Alexander and J. Augustynski, in *On Solar Hydrogen and Nanotechnology*, ed. L. Vayssieres, John Wiley & Sons, Singapore, 2009, pp. 333-346.
6. K. Sivula, F. Le Formal and M. Graetzel, *ChemSusChem*, 2011, **4**, 432-449.
7. J. Brillet, J.-H. Yum, T. Hisatomi, R. Solarska, J. Augustynski, M. Graetzel and K. Sivula, *Nature Photonics*, 2012, **6**, 824-828.
8. K. R. Reyes-Gil, C. Wiggenhorn, B. S. Brunschwig and N. S. Lewis, *The Journal of Physical Chemistry C*, 2013, **117**, 14947-14957.
9. C. Santato, M. Odziemkowski, M. Ulmann and J. Augustynski, *Journal of the American Chemical Society* 2001, **123**, 10639-10640.
10. C. Santato, M. Ulmann and J. Augustynski, *The Journal of Phyisical Chemistry B*, 2001, **105**, 936-940.
11. R. Solarska, B. D. Alexander and J. Augustynski, *Journal of Solid State Electrochemistry*, 2004, **8**, 748-756.
12. J. H. Park and A. J. Bard, *Electrochemical and Solid-State Letters* 2006, **9**, E5-E8.
13. L. Meda, G. Tozzola, A. Tacca, G. L. Marra, S. Caramori, V. Cristino and C. A. Bignozzi, *Solar Energy Materials and Solar Cells*, 2010, **94**, 788-796.
14. N. R. de Tacconi, C. R. Chenthamarakshan, G. Yogeeswaran, A. Watcharenwong, R. S. de Zoysa, N. A. Basit and K. Rajeshwar, *The Journal of Phyisical Chemistry B*, 2006, **110**, 25347-22355.
15. A. Watcharenwong, W. Chanmanee, N. R. de Tacconi, C. R. Chenthamarakshan, P. Kajitvichyanukul and K. Rajeshwar, *Journal of Electroanalytical Chemistry*, 2008, **612**, 112.
16. R. Hahn, J. M. Macak and P. Schmuki, *Electrochemistry Communications*, 2007, **2007**, 947-952.
17. V. Cristino, S. Caramori, R. Argazzi, L. Meda, G. L. Marra and C. A. Bignozzi, *Langmuir*, 2011, **27**, 7276-7284.
18. M. F. Daniel, B. Desbat, J. C. Lassegues and R. Garie, *Journal of Solid State Chemistry*, 1988, **73**, 127-139.
19. A. Rougier, F. Portemer, A. Quédé and M. El Marssi, *Applied Surface Science*, 1999, **153**, 1-9.
20. M. Allaf Behbani, M. Ranjbar, P. Kameli and H. Salamati, *Sensors and Actuators B: Chemical*, 2013, **188**, 127-136.
21. G. Leftherotis, S. Papaefthimiou, P. Yianoulis and *Solar Energy Materials and Solar Cells* 2004, **83**, 115-124.
22. Y. Pihosh, I. Turkevych, K. Mawatari, J. Uemura, Y. Kazoe, S. Kosar, K. Makita, T. Sugaya, T. Matsui and D. Fujita, *Scientific reports*, 2015, **5**.
23. W. Li, F. Zhan, J. Li, C. Liu, Y. Yang, Y. Li and Q. Chen, *Electrochimica Acta*, 2015, **160**, 57.

24. Y. Liu, J. Li, W. Li, Y. Yang, Y. Li and Q. Chen, *The Journal of Physical Chemistry C*, 2015, **119**, 14834-14842.
25. W. Mu, X. Xie, R. Zhang, Q. Yu, K. Ly, H. Wei and Y. Jian, *RSC Advances*, 2014, **4**, 36064-36070.
26. Y. Liu, J. Li, W. Li, Q. Liu, Y. Yang, Y. Li and Q. Chen, *International Journal of Hydrogen Energy*, 2015, **40**, 8856-8863.
27. T. Zhang, Z. Zhu, H. Chen, Y. Bai, S. Xiao, X. Zheng, Q. Xue and S. Yang, *Nanoscale*, 2015, **7**, 2933-2940.
28. B. M. Klepser and B. M. Bartlett, *Journal of the American Chemical Society*, 2014, **136**, 1694-1697.
29. J. K. Kim, K. Shin, S. M. Cho, T.-W. Lee and J. H. Park, *Energy & Environmental Science*, 2011, **4**, 1465-1470.
30. Q. Mi, A. Zhanaidarova, B. S. Brunschwig, H. B. Gray and N. S. Lewis, *Energy & Environmental Science*, 2012, **5**, 5694-5700.
31. J. C. Hill and K.-S. Choi, *The Journal of Physical Chemistry C*, 2012, **116**, 7612-7620.
32. Z. Chen, F. T. Jaramillo, T. G. Deutsch, A. Kleimann-Shwarstein, A. J. Forman, N. Gaillard, R. Garland, K. Takanabe, C. Heske, M. Sunkara, E. W. McFarland, K. Domen, E. L. Miller, J. A. Turner, H. N. Dinh and *Journal of Materials Research* 2010, **25**, 3-16.
33. N. Dalle Carbonare, V. Cristino, S. Berardi, S. Carli, R. Argazzi, S. Caramori, L. Meda, A. Tacca and C. A. Bignozzi, *ChemPhysChem*, 2014, **6**, 1164-1174.
34. S. Caramori, V. Cristino, L. Meda, A. Tacca, R. Argazzi and C. A. Bignozzi, *Energy Procedia*, 2012, **22**, 127-136.
35. A. Tacca, L. Meda, G. Marra, A. Savoini, S. Caramori, V. Cristino, C. A. Bignozzi, V. Gonzalez Pedro, P. P. Boix, S. Gimenez and J. Bisquert, *Chem.Phys.Chem*, 2012, **13**, 3025-3034.
36. C. A. Bignozzi, S. Caramori, V. Cristino, R. Argazzi, L. Meda and A. Tacca, *Chemical Society Reviews*, 2013, **4**, 2228-2246.
37. R. Solarska, R. Jurczakowski and J. Augustynski, *Nanoscale*, 2012, **4**, 1553-1556.
38. G. R. Buettner, *Free Radic. Biology & Medicine*, 1987, **3**, 259-303.
39. A. Molinari, R. Argazzi and A. Maldotti, *Journal of Molecular Catalysis.A:Chemistry*, 2013, **372**, 23-28.
40. H. Czili and A. Horvath, *Appl.Catal.B:Environ.*, 2008, **81**, 295-302.
41. A. Valdes and G.-J. Kroes, *The Journal of Chemical Physics*, 2009, **130**, 114701-114709.
42. C. Hitz and A. Lasia, *Journal of Electroanalytical Chemistry*, 2001, **500**, 213-222.
43. L. Bertoluzzi, P. Lopez-Varo, J. A. J. Tejada and J. Bisquert, *Journal of Materials Chemistry A*, 2015, **DOI: 10.1039/C5TA03210E**.
44. S. R. Biaggio, R. C. Rocha-Filho, J. R. Vilche, F. E. Varela and L. M. Gassa, *Electrochimica Acta*, 1997, **42**, 1751-1758.
45. J. Zhao, E. Olide and F. E. Osterloh, *Journal of Electrochemical Society*, 2015, **162**, H65-H71.
46. F. M. Pesci, A. J. Cowan, B. D. Alexander, J. R. Durrant and D. R. Klug, *The Journal of Physical Chemistry Letters*, 2011, **2**, 1900-1903.
47. W. Kim, T. Tachikawa, D. Monllor-Satoca, H.-i. Kim, T. Majima and W. Choi, *Energy & Environmental Science*, 2013, **6**, 3732-3739.

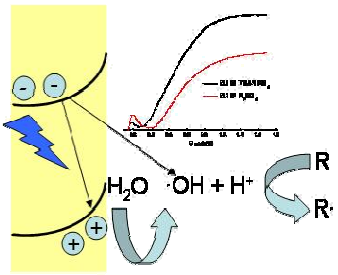

Charge transfer Dynamics in WO_3 photoelectrodes: hydroxyl radicals are the primary water oxidation intermediates generated via valence band hole injection.